Journal of Materials Chemistry C

ROYAL SOCIETY OF CHEMISTRY

PAPER

View Article Online
View Journal | View Issue

Cite this: J. Mater. Chem. C, 2025, 13, 5719

Enhanced three-photon absorption excited at near-infrared laser pulses and stability of $MAPbBr_3$ quantum dots encapsulated in mesoporous single MOF-5 crystals†

Wenqing Wang,‡[a] Renhua Liu,‡[b] Shaowen Zhu,[a] Minjie Zhou,[c] Bing Jin,[d] Shunbin Lu,*[b] Min Liu,*[a] Xuantao Su*[a] and Wei Ji[be]

Received 2nd December 2024,
Accepted 23rd January 2025

DOI: 10.1039/d4tc05087h

rsc.li/materials-c

Organometallic halide perovskites have attracted attention due to their excellent optical properties. However, the inherent instability limits their wide application in the field of optoelectronics. In this study, a distribution immersion method was used to embed $MAPbBr_3$ perovskite quantum dots into mesoporous MOF-5 microcrystals, constructing an effective host–guest structure. Compared with $MAPbBr_3$ quantum dots, the $MAPbBr_3$@MOF-5 composite not only exhibits superior optical performance but also significantly enhanced long-term stability and thermal stability. Nonlinear optical analysis shows that under the excitation of near-infrared femtosecond laser pulses, the $MAPbBr_3$@MOF-5 composite exhibits significantly enhanced multiphoton absorption capability. Notably, its effective three-photon absorption coefficient ($\alpha_3\eta \approx (27.4 \pm 3.1) \times 10^{-5}$ cm^3 GW^{-2}) is an order of magnitude larger than that of $MAPbBr_3$. These outstanding characteristics indicate that the $MAPbBr_3$@MOF-5 composite has great potential for applications in photonics and information communication, especially in the manufacture of multifunctional nonlinear optical devices and future micro–nano photonic integration technologies.

Introduction

Hybrid organic–inorganic halide perovskite materials, such as $MAPbX_3$ (X = Cl, Br, I), have garnered significant attention due to their potential applications in various fields. These materials exhibit exceptional optoelectronic properties, making them highly promising for use in solar cells, light-emitting diodes (LEDs), lasers, photodetectors, and multifunctional sensors.[1–5] Recently, colloidal perovskite $MAPbX_3$ nanocrystals (NCs), also known as quantum dots (QDs), have been attracting attention due to their excellent luminescent properties, which include high photoluminescence (PL) quantum yields, tunable emission wavelengths, short-radiative lifetimes, and narrow-band emissions.[6–8] In addition to excellent linear optical properties, $MAPbX_3$ NCs also exhibit remarkable nonlinear optical (NLO) responses.[9,10] Among them, multi-photon excited photoluminescence (MPEPL) is particularly prominent. MPEPL involves the absorption of multiple photons, causing an electron to jump from the ground state to the excited state while leaving a hole in the ground state. Subsequently, the electron relaxes to the lowest energy level of the excited state and radiatively recombines with the hole in the ground state. MPEPL has a wide range of applications in the fields of optoelectronics, transmission of photonic signals and biomedicine.[11,12] However, although $MAPbX_3$ exhibits excellent performance, its practical applications are limited by the instability of organic cations, which are prone to rapid degradation under conditions such as moisture, UV radiation, oxygen and high temperature.[13] Therefore, an improvement in the stability of perovskite quantum dots is a key challenge in realizing their optical applications. One feasible solution is to design and fabricate hybrid composite materials incorporating perovskite QDs.

Metal–organic frameworks (MOFs) are a class of porous crystalline materials with fascinating properties, including tunable pore sizes and high specific surface areas. These characteristics make them promising platforms for host–guest

[a] School of Integrated Circuits, Shandong University, Jinan 250100, China. E-mail: xtsu@sdu.edu.cn, liumin@sdu.edu.cn
[b] International Collaborative Laboratory of 2D Materials for Optoelectronic Science & Technology of Ministry of Education, Institute of Microscale Optoelectronics (IMO), Shenzhen University, Shenzhen 518060, China. E-mail: shunbin_lu@szu.edu.cn
[c] Center for Optics and Research Engineer, Key Laboratory of Laser and Infrared System, Ministry of Education, Shandong University, Qingdao 266237, China
[d] Institute of Frontier Chemistry, School of Chemistry and Chemical Engineering, Shandong University, Qingdao 266237, China
[e] Department of Physics, National University of Singapore, Singapore 117551, Singapore

† Electronic supplementary information (ESI) available. See DOI: https://doi.org/10.1039/d4tc05087h

‡ Both Wenqing Wang and Renhua Liu contributed equally to this manuscript.

chemistry.[14–16] MOFs can be conveniently designed and self-assembled to provide ideal host environments for various guest species.[17–19] MOF-5 ($C_{24}H_{12}O_{13}Zn_4$) features a three-dimensional structure and is characterized by its high specific surface area, significant porosity, and exceptional thermal stability.[20] In comparison to MOFs with one- or two-dimensional structures, such as MOF-8,[21] which is defined by its one-dimensional chain structure, MOF-5 offers a more comprehensive platform for exploring the influence of pore size on doped quantum dots and was therefore selected for this study. There have been reports of integrating various QDs into MOFs to develop novel composite materials with superior combined properties compared to their individual components.[22] Although there have been studies on loading perovskite $MAPbX_3$ QDs into different hosts to enhance their stability, a more extensive exploration for improving the stability of these materials is still needed.[15,23,24] The fundamental properties, mechanisms, and nonlinear optical characteristics of $MAPbX_3$ QDs encapsulated in MOFs remain relatively unexplored.

Here, we report a stepwise impregnation method to embed perovskite $MAPbBr_3$ QDs into mesoporous MOF-5 single crystals. Compared to $MAPbBr_3$ QDs, the resulting $MAPbBr_3$@MOF-5 composite materials exhibited improved long-term storage stability and high thermal stability. Moreover, we found that the three-photon absorption coefficient of $MAPbBr_3$@MOF-5 was significantly enhanced compared to $MAPbBr_3$ microcrystals.[25,26] This enhancement is attributed to the strong confinement and surface passivation provided by the MOF-5 framework.

Experimental section

The preparation process of the $MAPbBr_3$@MOF-5 composite is shown in Scheme 1, which includes three steps: (a) synthesis of mesoporous MOF-5 microcrystals by a solvothermal method, (b) introduction of Pb^{2+} into the pores of MOF-5 by an immersion method, and (c) addition of Pb^{2+}@MOF-5 to MABr solution to facilitate the formation of perovskite quantum dots within the pores of MOF-5.

The structure of $MAPbBr_3$@MOF-5 was characterized by scanning electron microscopy (SEM), powder X-ray diffraction (XRD), and transmission electron microscopy (TEM). To test the thermal stability, thermogravimetric analysis (TGA) was performed on $MAPbBr_3$@MOF-5. Additionally, PL, time-resolved PL, and absorption spectra were measured.

Detailed information on the materials and chemicals used, synthesis of MOF-5, $MAPbBr_3$, and the $MAPbBr_3$@MOF-5 composite, detection methodology, and instrumental techniques can be found in the ESI.†

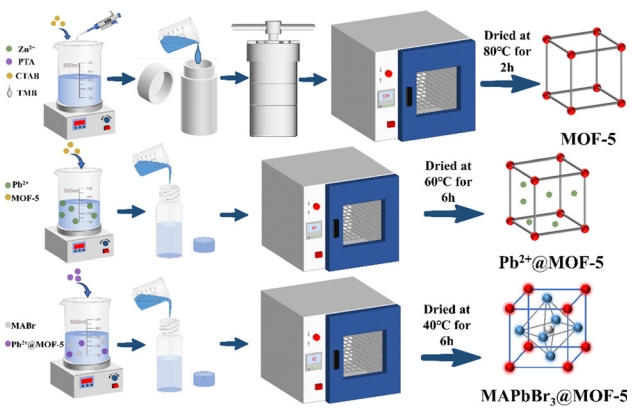

Scheme 1 Synthesis process of $MAPbBr_3$@MOF-5.

Results and discussion

MOF-5 is an excellent metal–organic framework material composed of PTA and tetrahedral ZnO_4 units, featuring high porosity and good stability. The microporous MOF-5 is synthesized by dissolving $Zn(NO_3)_2{\cdot}6H_2O$ and PTA in a DMF solution and heating at 135 °C for 24 hours. Its micropore sizes are about 1.85 nm,[27] which limits the encapsulation of $MAPbBr_3$ into MOF-5. Therefore, in order to obtain mesoporous MOF-5 crystals, CTAB and TMB were used as templating agents in this work to expand the porosity of the MOF-5 microcrystals. CTAB occupies the pore channels of the MOF-5 microcrystals, and TMB further expands the pore channel sizes by swelling CTAB micelles, thereby increasing the pore sizes of the MOF-5 microcrystals.[20,28] By changing the molar ratios of the reactants, we synthesized a series of MOF-5 microcrystals and studied the changes in PL intensity of $MAPbBr_3$ encapsulated in MOF-5 microcrystals synthesized with different reactant molar ratios (Fig. S1, ESI†). When the molar ratio is 1 : 2 for CTAB to TMB, the PL intensity of the hybrid material is the strongest compared to other ratios after encapsulating $MAPbBr_3$ QDs. This may be attributed to the fact that MOF-5 synthesized using this molar ratio has the highest mesoporous porosity and the most suitable mesoporous pore size. The introduction of CTAB can expand the mesoporous volume of MOF-5, but this expansion is limited. Then, using TMB to swell CTAB micelles can significantly increase the pore volume. However, excessive addition of TMB may damage the porous structure of the MOF-5 crystals.[20] Therefore, there is an optimal molar ratio to achieve the best encapsulation of $MAPbBr_3$ QDs. Further confirmation of the effect of CTAB and TMB addition on the pore expansion of the MOF-5 samples was achieved through characterization by XRD and SEM. As shown in Fig. S2 (ESI†), the XRD pattern of the treated MOF-5 sample deviates from that of the theoretical MOF-5 and some impurity peaks can be observed. This may be attributed to the increase in pore size of the treated MOF-5, which consequently leads to changes in its crystal structure, including the introduction of defects (Fig. S2(a), ESI†).[20] After CTAB is embedded, the MOF particles maintain their cubic morphology, but larger cavities are observed within the particles (Fig. S2(b), ESI†), indicating effective expansion of the internal pore structure.

In Fig. 1(a), the XRD pattern of $MAPbBr_3$@MOF-5 is shown. Both the XRD peaks of MOF-5 and $MAPbBr_3$ in the XRD pattern of $MAPbBr_3$@MOF-5 were observed. After embedding QDs, $MAPbBr_3$@MOF-5 demonstrated peaks of 14.82°, 30.00°,

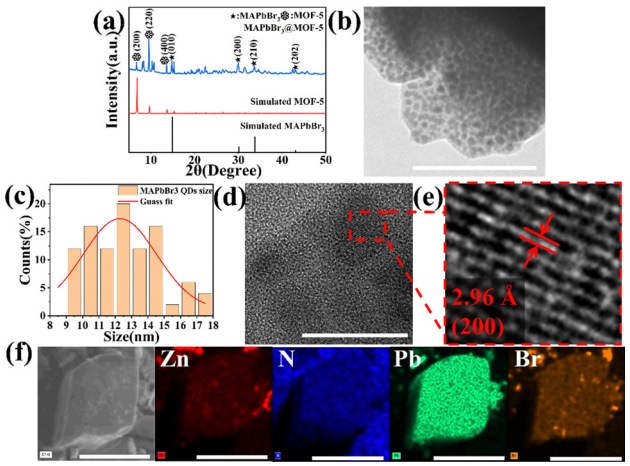

Fig. 1 Structure characterization. (a) XRD patterns of $MAPbBr_3$@MOF-5. (b) TEM (scale bar: 100 nm) and (c) histogram of $MAPbBr_3$ particle size distribution with Gauss fitting. (d) and (e) HRTEM of $MAPbBr_3$@MOF-5 (scale bar, 20 nm). (f) SEM mapping of elements (Zn, N, Pb and Br) in $MAPbBr_3$@MOF-5 (scale bar, 20 μm).

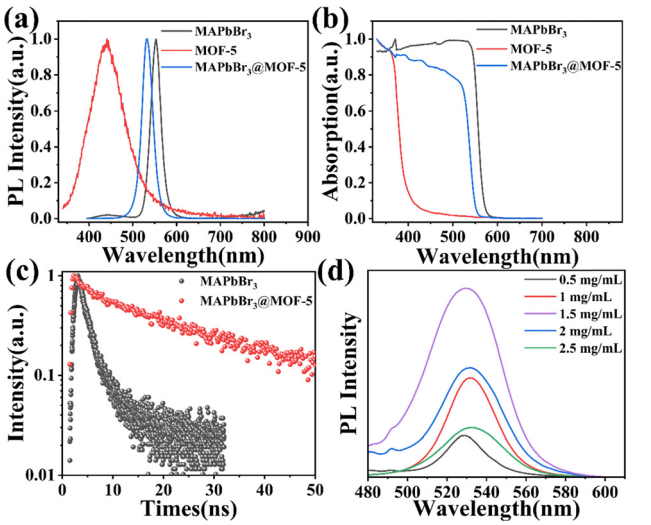

Fig. 2 (a) The normalized PL spectra, (b) the UV-Vis absorption, (c) the PL decay plots of $MAPbBr_3$@MOF-5 and $MAPbBr_3$ and (d) the PL spectra of $MAPbBr_3$@MOF-5 synthesized with varying concentrations of MABr.

33.64° and 43.06° corresponding to the planes of (010), (200), (210) and (202) of $MAPbBr_3$, respectively. The TEM image (Fig. 1(b)) shows that the PeQDs are embedded in the holes of MOF-5. Based on the size distribution histogram and Gauss fitting of $MAPbBr_3$ QDs (Fig. 1(c)), the average size of the QD particles is 12 nm. The average size of the QDs in other regions, as determined from the TEM results, is shown in Fig. S2(c–f) (ESI†). The HRTEM images are shown in Fig. 1(d and e). The interplanar distance from the fringes is 2.96 Å, which could be attributed to the (200) planes of the $MAPbBr_3$. The SEM mapping images, as shown in Fig. 1(f), show the uniform distribution of the four elements, indicating the coexistence of the $MAPbBr_3$ QDs and MOF-5. The inset of Fig. S2(b) (ESI†) displays an image of the $MAPbBr_3$@MOF-5 sample. Fig. S3 (ESI†) depicts the TGA analysis of $MAPbBr_3$@MOF-5, showing that when heated to 400 °C in a nitrogen atmosphere, the composite material experiences a mass loss of only 12.1%. The result indicates that $MAPbBr_3$@MOF-5 demonstrates good thermal stability and possesses a high decomposition temperature.

The fluorescence properties of the synthesized $MAPbBr_3$@MOF-5 composite were subsequently analyzed. The PL spectra of $MAPbBr_3$ and $MAPbBr_3$@MOF-5 are shown in Fig. 2(a). After embedding QDs into MOF-5, the $MAPbBr_3$@MOF-5 composite exhibits a narrow green peak centered at 533 nm under UV excitation (375 nm). The narrow green peak of $MAPbBr_3$@MOF-5 can be attributed to the emission of $MAPbBr_3$ QDs. Compared to $MAPbBr_3$, the PL peak wavelength of $MAPbBr_3$ QDs in the $MAPbBr_3$@MOF-5 composite has a blue shift of 20 nm. The absorption spectra in Fig. 2(b) also show a blue shift in the absorption edges of $MAPbBr_3$@MOF-5 compared to $MAPbBr_3$ (more details can be found in the section titled 'Characterization' in ESI†). These properties can be attributed to the strong quantum confinement effect of perovskite QDs. When the size of metal halide perovskite QDs is reduced to the nanometer scale, the electronic band structure of the perovskite undergoes changes. Due to the quantum confinement effect, the emission peak shifts from green to blue.[29,30] The PL decay curves of $MAPbBr_3$@MOF-5 and $MAPbBr_3$ monitored at 533 nm under UV light (375 nm) excitation are shown in Fig. 2(c). The PL decay of $MAPbBr_3$@MOF-5 can be described by a bi-exponential fit.[31] The average fluorescence lifetime of $MAPbBr_3$ increased from 2.4 ns to 28.5 ns for $MAPbBr_3$@MOF-5. Fig. S4(a) (ESI†) illustrates the variation of the photoluminescence (PL) lifetime within the temperature range from 300 to 430 K and the derived lifetime decreases from 43.6 ns to 5.5 ns, as shown in Fig. S4(b) (ESI†).[32,33] As the temperature increases, the thermal excitation drives the lattice structure to undergo distortion. Simultaneously, the generation of thermal defects initiates a pronounced non-radiative recombination process.[34] The non-radiative decay rate of $MAPbBr_3$@MOF-5 rises with increasing temperature. This elevated non-radiative decay rate results in a significant reduction in the PL lifetime. It is well-known that the PL decay of perovskite materials is often attributed to radiative and non-radiative recombination processes of excitons, with non-radiative recombination typically associated with short lifetimes in the lifetime fitting.[35] The extended lifetime may be attributed to surface passivation, which reduces the nonradiative relaxation of surface traps in encapsulated $MAPbBr_3$ QDs.[36–38] Additionally, there is significant spectral overlap between the emission of MOF-5 crystals and the absorption of $MAPbBr_3$ QDs. Therefore, energy transfer from MOF-5 crystals to $MAPbBr_3$ QDs is expected to occur in $MAPbBr_3$@MOF-5.[39] Moreover, by adjusting the concentration of MABr, we can manipulate the emission of $MAPbBr_3$@MOF-5. Fig. 2(d) displays a series of PL spectra for $MAPbBr_3$@MOF-5, showing that as the concentration of MABr increases (0.5, 1, 1.5, 2, 2.5 mg mL^{-1}), the PL intensity at first increases and then decreases, reaching a maximum at a concentration of 1.5 mg mL^{-1}. As the concentration of MABr increases, the amount of $MAPbBr_3$ QDs in the $MAPbBr_3$@MOF-5 composite

rises, leading to a proportional enhancement of the composite's photoluminescence (PL) intensity. However, if the amount of MABr added exceeds a certain threshold, quantum dots aggregation may occur, resulting in a reduction in PL intensity.

Notably, we have observed a substantial improvement in the stability of the $MAPbBr_3$@MOF-5 composite material. We performed thermal stability tests and long-term stability tests on the composite material and compared the results with those of $MAPbBr_3$ powder. As shown in Fig. 3(a), $MAPbBr_3$@MOF-5 maintained 49.3% of its original photoluminescence (PL) intensity at 55 °C, and even still emitted light at 125 °C. After 90 days of exposure to air at room temperature, $MAPbBr_3$@MOF-5 retained 63.9% of its initial PL intensity, whereas the $MAPbBr_3$ QDs showed complete quenching after 14 days (Fig. 3(b)). Based on these results, we can conclude that the $MAPbBr_3$@MOF-5 composite is significantly more stable in air and at high temperatures compared to $MAPbBr_3$ PeQDs.

Under excitation by near-infrared femtosecond laser pulses, $MAPbBr_3$@MOF-5 demonstrates excellent MPEPL (more experimental details can be found in the section titled 'Multi-photon excited photoluminescence' in the ESI†). Fig. S5 (ESI†) illustrates the schematic diagram of the multi-photon excitation photoluminescence measurements. Fig. 4(a and b) shows the MPEPL spectra of the $MAPbBr_3$@MOF-5 sample under excitation at 800 nm for 2-photon absorption (2PA) and 1200 nm for 3-photon absorption (3PA), respectively. The relationship between PL intensity and pump intensity exhibits the characteristics of multiphoton absorption. The insets of Fig. 4(a and b) show that the slopes are 2.02 at 800 nm and 3.04 at 1200 nm, indicating 2PA and 3PA, respectively. Fig. S6 (ESI†) presents the MPEPL spectra of the $MAPbBr_3$ sample under excitation at 800 nm for 2PA and 1200 nm for 3PA, respectively. The insets of Fig. S6(a) and (b) (ESI†) display that the slopes are 1.99 at 800 nm and 2.96 at 1200 nm, indicating 2PA and 3PA, respectively.

The MPEPL signal was collected and processed according to previous reports.[25,31] The multiphoton absorption cross section (σ_n) and multiphoton absorption coefficient (α_n) can be converted:[40]

$$\sigma_n \rho = \frac{(\hbar\omega)^{n-1}\alpha_n}{N_A}$$

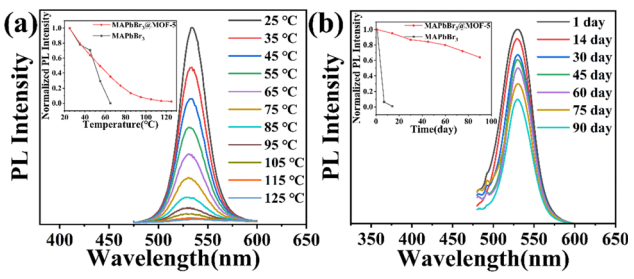

Fig. 3 Thermal stability test (a) and long-term storage stability test (b) of $MAPbBr_3$@MOF-5. Insets: Normalized PL intensity as a function of experimental temperature (a) and storage time (b) for $MAPbBr_3$@MOF-5 (red line) and $MAPbBr_3$ (black line).

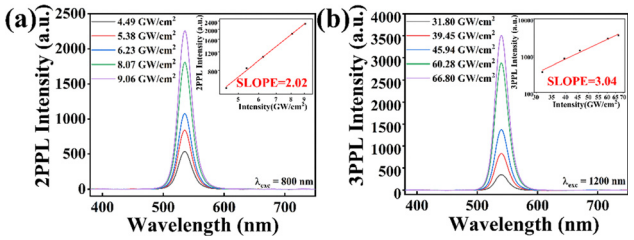

Fig. 4 Multiphoton-excited photoluminescence (MPEPL) of $MAPbBr_3$@MOF-5. (a) 2PPL spectra at 800 nm, and (b) 3PPL spectra at 1200 nm.

In the above equation, σ_n is the n-photon-absorption cross section; ρ is the sample molar concentration; $\hbar\omega$ is the photon energy of the incident laser beam; α_n is the n-photon-absorption coefficient; N_A is Avogadro's constant.

Using the above formulas, the effective multiphoton absorption coefficients ($\alpha_3\eta$) of $MAPbBr_3$@MOF-5 are calculated to be $\alpha_2\eta \approx (1.23 \pm 0.05)$ cm GW^{-1} for 2PA (800 nm), and $\alpha_3\eta \approx (27.4 \pm 3.1) \times 10^{-5}$ cm^3 GW^{-2} for 3PA (1200 nm). Table 1 shows that the $\alpha_2\eta$ of $MAPbBr_3$@MOF-5 remains at the same level as perovskites, and the $\alpha_3\eta$ of $MAPbBr_3$@MOF-5 is an order of magnitude higher than that of perovskites. Moreover, the consistency of $\alpha_n\eta$ for $MAPbBr_3$@MOF-5 across different excitation intensities highlights its outstanding performance, especially in three-photon frequency conversion.

This result indicated the influence of the MOF-5 framework in confining $MAPbBr_3$ QDs and providing protection, significantly enhancing their nonlinear optical properties. Recent studies have shown that due to variations in surface free energy, PeQDs tend to nucleate and grow within the pores of MOFs, as this process can reduce the energy barrier and critical radius.[31,44] Without the confinement of pores, PeQDs would aggregate and cause fluorescence quenching. When $MAPbBr_3$ is encapsulated into MOF-5, its growth is restricted by the pores of MOF-5, leading to more effective surface passivation. The quantum confinement effect will significantly impact the band structure and dielectric properties of PeQDs, leading to substantial changes in the multiphoton absorption coefficient.[45] This surface passivation can reduce nonradiative recombination at the surface traps and increase the probability of multiphoton transitions.[46–48] Additionally, the presence of local field effects may enhance the nonlinear optical properties of the composite.[46] Above all, interfacial energy transfer from transition-metal ions (Zn^{2+}) may enhance their optical performance.[49] Therefore, $MAPbBr_3$ QDs encapsulated in MOF-5 exhibit a significantly enhanced multiphoton absorption coefficient.

Conclusions

In summary, we have successfully embedded $MAPbBr_3$ QDs into the pores of mesoporous MOF-5 through a stepwise immersion strategy. The resulting $MAPbBr_3$@MOF-5 composites not only exhibit excellent optical performance but also demonstrate outstanding long-term stability and thermal stability. Furthermore, the confinement and surface passivation

Table 1 Comparison of effective multiphoton absorption coefficients, $\alpha_n\eta$, of $MAPbBr_3$, $MAPbI_3$ and $MAPbBr_3$@MOF-5

Multiphoton excitation	$\alpha_n\eta$ (cm GW^{-1}) (at 800 nm)	$\alpha_3\eta$ (10^{-5} cm^3 GW^{-2}) (at 1200 nm)	
$MAPbBr_3$@MOF-5	1.23 ± 0.05	27.4 ± 3.1	This work
$MAPbBr_3$ single crystal	7.35 ± 0.21		Ref. 9,10,25 and 41
$MAPbBr_3$ micro crystal		1.90	Ref. 25 and 26
$MAPbI_3$ single crystal	9.2	1.33	Ref. 9,42 and 43

offered by the MOF-5 framework significantly enhance the nonlinear optical properties of the composites. Specifically, the two-photon absorption coefficient of $MAPbBr_3$@MOF-5 is comparable to that of pure $MAPbBr_3$ perovskite, while its three-photon absorption coefficient is an order of magnitude greater than that of the pure perovskite. Given its exceptional optical characteristics and high stability, the $MAPbBr_3$@MOF-5 composites present great potential for applications in biomedicine, optoelectronic devices, and future photonic integration technologies.

Data availability

The data supporting this article have been included as part of the ESI.†

Conflicts of interest

The authors declare no competing financial interest.

Acknowledgements

This work is supported by the STI 2030-Major Project (2022ZD0209900), the National Natural Science Foundation of China (No. 11904206), the Instrument Improvement Funds of Shandong University Public Technology Platform (ts20230103), the Shenzhen Science and Technology Program (JCYJ202205 31103016036), and the Shenzhen Key Laboratory of 2D Metamaterials for Information Technology (ZDSYS20170727 1014468).

Notes and references

1 F. Arabpour Roghabadi, M. Alidaei, S. M. Mousavi, T. Ashjari, A. S. Tehrani, V. Ahmadi and S. M. Sadrameli, *J. Mater. Chem. A*, 2019, **7**, 5898–5933.
2 H. Zhang, T. Yu, C. Wang, R. Jia, A. A. A. Pirzado, D. Wu, X. Zhang, X. Zhang and J. Jie, *ACS Nano*, 2022, **16**, 6394–6403.
3 G. Xing, N. Mathews, S. S. Lim, N. Yantara, X. Liu, D. Sabba, M. Grätzel, S. Mhaisalkar and T. C. Sum, *Nat. Mater.*, 2014, **13**, 476–480.
4 H. R. Jung, Y. Cho and W. Jo, *Adv. Opt. Mater.*, 2022, **10**, 2102175.
5 X. Wu, B. Zhou, J. Zhou, Y. Chen, Y. Chu and J. Huang, *Small*, 2018, **14**, 1800527.
6 Q. V. Le, K. Hong, H. W. Jang and S. Y. Kim, *Adv. Electron. Mater.*, 2018, **4**, 1800335.
7 H.-C. Wang, Z. Bao, H.-Y. Tsai, A.-C. Tang and R.-S. Liu, *Small*, 2018, **14**, 1702433.
8 H. Huang, A. S. Susha, S. V. Kershaw, T. F. Hung and A. L. Rogach, *Adv. Sci.*, 2015, **2**, 1500194.
9 F. O. Saouma, D. Y. Park, S. H. Kim, M. S. Jeong and J. I. Jang, *Chem. Mater.*, 2017, **29**, 6876–6882.
10 T.-C. Wei, S. Mokkapati, T.-Y. Li, C.-H. Lin, G.-R. Lin, C. Jagadish and J.-H. He, *Adv. Funct. Mater.*, 2018, **28**, 1707175.
11 R. Medishetty, J. K. Zaręba, D. Mayer, M. Samoć and R. A. Fischer, *Chem. Soc. Rev.*, 2017, **46**, 4976–5004.
12 R. Shi, X. Han, J. Xu and X.-H. Bu, *Small*, 2021, **17**, 2006416.
13 G. Niu, X. Guo and L. Wang, *J. Mater. Chem. A*, 2015, **3**, 8970–8980.
14 K. J. Lee, J. H. Lee, S. Jeoung and H. R. Moon, *Acc. Chem. Res.*, 2017, **50**, 2684–2692.
15 C. Zhang, B. Wang, W. Li, S. Huang, L. Kong, Z. Li and L. Li, *Nat. Commun.*, 2017, **8**, 1138.
16 H. Wu, P. Ran, L. Yao, H. Cai, W. Cao, Y. Cui, Y. Michael Yang, D. Yang and G. Qian, *Chem. Eng. J.*, 2024, **491**, 152098.
17 S. Cao, G. Gody, W. Zhao, S. Perrier, X. Peng, C. Ducati, D. Zhao and A. K. Cheetham, *Chem. Sci.*, 2013, **4**, 3573–3577.
18 K. Shen, L. Zhang, X. Chen, L. Liu, D. Zhang, Y. Han, J. Chen, J. Long, R. Luque, Y. Li and B. Chen, *Science*, 2018, **359**, 206–210.
19 L.-G. Qiu, T. Xu, Z.-Q. Li, W. Wang, Y. Wu, X. Jiang, X.-Y. Tian and L.-D. Zhang, *Angew. Chem., Int. Ed.*, 2008, **47**, 9487–9491.
20 J. Ren, T. Li, X. Zhou, X. Dong, A. V. Shorokhov, M. B. Semenov, V. D. Krevchik and Y. Wang, *Chem. Eng. J.*, 2019, **358**, 30–39.
21 W.-K. Jiang, T.-T. Huang, D.-X. Lv, Z.-H. Zhu, H.-H. Zou and F.-P. Liang, *Cryst. Growth Des.*, 2024, **24**, 9692–9700.
22 S. Jin, H.-J. Son, O. K. Farha, G. P. Wiederrecht and J. T. Hupp, *J. Am. Chem. Soc.*, 2013, **135**, 955–958.
23 S. Huang, Z. Li, L. Kong, N. Zhu, A. Shan and L. Li, *J. Am. Chem. Soc.*, 2016, **138**, 5749–5752.
24 D. Zhang, Y. Xu, Q. Liu and Z. Xia, *Inorg. Chem.*, 2018, **57**, 4613–4619.
25 W. Chen, S. Bhaumik, S. A. Veldhuis, G. Xing, Q. Xu, M. Grätzel, S. Mhaisalkar, N. Mathews and T. C. Sum, *Nat. Commun.*, 2017, **8**, 15198.
26 Y. Gao, S. Wang, C. Huang, N. Yi, K. Wang, S. Xiao and Q. Song, *Sci. Rep.*, 2017, **7**, 45391.
27 H. Li, M. Eddaoudi, M. O'Keeffe and O. M. Yaghi, *Nature*, 1999, **402**, 276–279.
28 C. Vautier-Giongo and H. O. Pastore, *J. Colloid Interface Sci.*, 2006, **299**, 874–882.
29 V. Malgras, S. Tominaka, J. W. Ryan, J. Henzie, T. Takei, K. Ohara and Y. Yamauchi, *J. Am. Chem. Soc.*, 2016, **138**, 13874–13881.

30 D. N. Dirin, L. Protesescu, D. Trummer, I. V. Kochetygov, S. Yakunin, F. Krumeich, N. P. Stadie and M. V. Kovalenko, *Nano Lett.*, 2016, **16**, 5866–5874.
31 Q. Fan, Z. Yan, H. Zhou, Y. Yao, Z. Wang, Y. Gao, Y. Wang, S. Lu, M. Liu and W. Ji, *J. Mater. Chem. C*, 2023, **11**, 5788–5795.
32 M.-H. Yu, D. Zhao, R.-J. Zhang, Q.-X. Yao, L. Jia and Q. Zong, *Ceram. Int.*, 2024, **50**, 11766–11775.
33 Y.-X. Bi, D. Zhao, R.-J. Zhang, L. Jia and Q. Zong, *Microchem. J.*, 2024, **205**, 111375.
34 J. Zheng, G. Yue, Z. A. Zhou, H. Li, L. Hou, C. Sun, X. Li, L. Kang, N. Wang, Y. Zhao and S. Zhou, *Adv. Funct. Mater.*, 2023, **33**, 2300607.
35 J. Wang, D. Huang, Y. Zhou, C. Liao, P. Guo, Z. Li, G. Zhou, X. Yu and J. Hu, *Small Struct.*, 2023, **4**, 2200391.
36 D. Zhang, W. Zhou, Q. Liu and Z. Xia, *ACS Appl. Mater. Interfaces*, 2018, **10**, 27875–27884.
37 X. Xiang, J. Li, J. Xue and Z. Fu, *Langmuir*, 2023, **39**, 5315–5322.
38 Z. Xie, X. Li, R. Li, S. Lu, W. Zheng, D. Tu, Y. Feng and X. Chen, *Nanoscale*, 2020, **12**, 17113–17120.
39 X. Jiang, J. Zhang, R. Fan, X. Zhou, K. Zhu and Y. Yang, *ACS Appl. Mater. Interfaces*, 2022, **14**, 49945–49956.
40 N. Liaros and J. T. Fourkas, *Laser Photonics Rev.*, 2017, **11**, 1700106.
41 G. Walters, B. R. Sutherland, S. Hoogland, D. Shi, R. Comin, D. P. Sellan, O. M. Bakr and E. H. Sargent, *ACS Nano*, 2015, **9**, 9340–9346.
42 F. Chun, B. Zhang, Y. Li, W. Li, M. Xie, X. Peng, C. Yan, Z. Chen, H. Zhang and W. Yang, *Chem. Eng. J.*, 2020, **399**, 125715.
43 D. Yang, C. Xie, J. Sun, H. Zhu, X. Xu, P. You, S. P. Lau, F. Yan and S. F. Yu, *Adv. Opt. Mater.*, 2016, **4**, 1053–1059.
44 C. Ren, Z. Li, L. Huang, X. Xiong, Z. Nie, Y. Yang, W. Zhu, W. Yang and L. Wang, *Nanoscale*, 2022, **14**, 4216–4224.
45 F. Zhou, X. Ran, D. Fan, S. Lu and W. Ji, *Adv. Opt. Mater.*, 2021, **9**, 2100292.
46 H. He, Y. Cui, B. Li, B. Wang, C. Jin, J. Yu, L. Yao, Y. Yang, B. Chen and G. Qian, *Adv. Mater.*, 2019, **31**, 1806897.
47 S. A. Veldhuis, Y. K. E. Tay, A. Bruno, S. S. H. Dintakurti, S. Bhaumik, S. K. Muduli, M. Li, N. Mathews, T. C. Sum and S. G. Mhaisalkar, *Nano Lett.*, 2017, **17**, 7424–7432.
48 B. H. Zhu, H. C. Zhang, J. Y. Zhang, Y. P. Cui and Z. Q. Zhou, *Appl. Phys. Lett.*, 2011, **99**, 021908.
49 S. Mollick, T. N. Mandal, A. Jana, S. Fajal and S. K. Ghosh, *Chem. Sci.*, 2019, **10**, 10524–10530.

